Steel and Composite Structures, *Vol. 32, No. 5 (2019) 657-670*
DOI: https://doi.org/10.12989/scs.2019.32.5.657

A fiber beam element model for elastic-plastic analysis of girders with shear lag effects

Wu-Tong Yan [1a], Bing Han [*1,2], Li Zhu [1b], Yu-Ying Jiao [1c] and Hui-Bing Xie [1d]

[1] *School of Civil Engineering, Beijing Jiaotong University, Beijing 100044, P.R. China*
[2] *Key Laboratory of Safety and Risk Management on Transport Infrastructures, Ministry of Transport, PRC, Beijing 100044, P.R. China*

(*Received April 17, 2019, Revised July 29, 2019, Accepted August 13, 2019*)

Abstract. This paper proposes a one-dimensional fiber beam element model taking account of materially non-linear behavior, benefiting the highly efficient elastic-plastic analysis of girders with shear-lag effects. Based on the displacement-based fiber beam-column element, two additional degrees of freedom (DOFs) are added into the proposed model to consider the shear-lag warping deformations of the slabs. The new finite element (FE) formulations of the tangent stiffness matrix and resisting force vector are deduced with the variational principle of the minimum potential energy. Then the proposed element is implemented in the OpenSees computational framework as a newly developed element, and the full Newton iteration method is adopted for an iterative solution. The typical materially non-linear behaviors, including the cracking and crushing of concrete, as well as the plasticity of the reinforcement and steel girder, are all considered in the model. The proposed model is applied to several test cases under elastic or plastic loading states and compared with the solutions of theoretical models, tests, and shell/solid refined FE models. The results of these comparisons indicate the accuracy and applicability of the proposed model for the analysis of both concrete box girders and steel-concrete composite girders, under either elastic or plastic states.

Keywords: fiber beam element; shear lag; elastic-plastic analysis; steel-concrete composite girder

1. Introduction

Concrete box girders and steel-concrete composite girders are widely used in expressway bridges, urban overpasses, and viaducts, and the shear-lag effects are non-negligible mechanical behaviors for these structures. Particularly, for girders with thin-walled and wide flanged sections, the shear lag effects are significant. The shear-lag effects are important issues in structural analysis and design because of their considerable influence on the structural stiffness and bearing capacity (Luo *et al*. 2019). An effective flange width is usually adopted to account for the effects during the initial structural design. However, the simplified effective flange width recommended by design codes are quite different from each other and sometimes may result in a significant error (Dezi *et al*. 2003). Therefore, an effective analytical model is needed to determine the structural stiffness and stress.

Elastic analysis models with the shear-lag effects have been a popular research topic for decades. Many analytical methods and models have been studied and proposed, such as the space grid analysis method (Ma *et al*. 2017), energy variational method (Chen *et al*. 2014, Lin *et al*. 2015, Reissner 1946, Zhou *et al*. 2018), and some numerical methods based on the FE model (Gara *et al*. 2009, Lacki *et al*. 2019, Zhang and Lin 2014, Zhou 2010). Reissner (1946) first proposed the shear-lag effect analysis method based on the minimum potential energy principle and variational method. Then, some researchers applied this method to concrete box girders (Lin *et al*. 2015, Zhou *et al*. 2018) and steel-concrete composite girders (Dezi *et al*. 2003, Zhu and Su 2017). Analytical formulas were proposed to address the different structural types with shear-lag effects. However, engineering structures are complex, and complicated analytical formulas are challenging to use in practice. Numerical models based on the FE method are an effective solution, and these models include the shell and solid FE models (Boules *et al*. 2018, Lacki *et al*. 2019). However, the complicated modeling process and enormous structural stiffness equations reduce the analysis efficiency for large-scale structures. In recent years, some researchers have proposed a beam element model with the shear-lag effects to improve analysis efficiency. There were two different ways to construct the shear-lag warping displacement field in the beam element. The first was to employ the homogeneous analytical solution based on the shear-lag differential equation as a shape function (Zhang and Lin 2014, Zhou 2010). The second used the Hermite polynomial interpolation method by piecewise approximation (Vojnić-Purčar *et al*. 2019), and Gara *et al*. (2009) verified the effectiveness and accuracy of this method.

Nevertheless, the cracking and crushing of concrete, as well as the plasticity of reinforcement materially non-linear behaviors, are inevitable under capacity limit states.

*Corresponding author, Professor,
E-mail: bhan@bjtu.edu.cn
[a] Ph.D. Student, E-mail: yanwutong@bjtu.edu.cn
[b] Professor, E-mail: zhuli@bjtu.edu.cn
[c] Ph.D. Student, E-mail: 14115295@bjtu.edu.cn
[d] Lecturer, E-mail: hbxie@bjtu.edu.cn

http://www.techno-press.org/?journal=scs&subpage=6 ISSN: 1229-9367 (Print), 1598-6233 (Online)

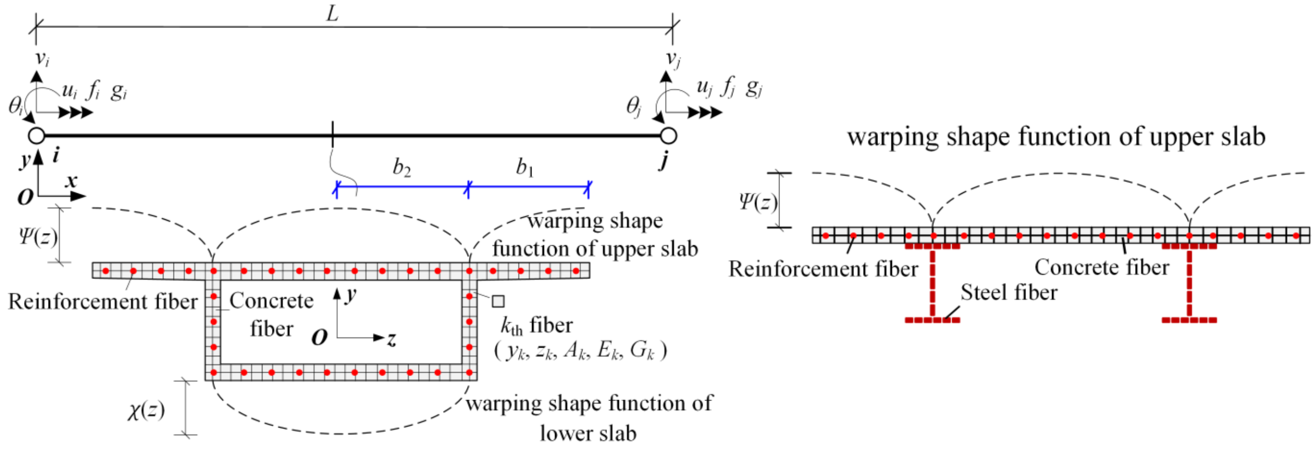

(a) Cross-section of concrete box girder (b) Cross-section of steel-concrete composite girder

Fig. 1 Fiber beam element with the shear-lag effect

Moreover, the shear-lag effect is constantly changing under elastoplastic loading states and a full range analysis model is needed. The aforementioned models are not applicable to these cases. Usually, the refined shell/brick element models are employed to accomplish the elastoplastic analysis, but these models come with high computational costs. Recently, some researchers tried to study the high-efficiency analysis model for structural elastic-plastic behavior that takes into consideration the shear-lag effects. Tao and Nie (2014) did excellent work for proposing the conventional fiber beam element with modified material constitutive laws to consider the slab spatial effect in steel-concrete composite frames.

In this paper, we develop a new fiber beam element model with consideration of the shear-lag effect and materially non-linear property without the modification of the material parameters. Consideration of economical computational cost, two DOFs are introduced into the proposed model to approximately describe the shear lag warping deformation. Based on the displacement-based fiber beam element, a novel 10-DOF element model considering the shear lag warping effects and materially non-linear behavior is developed. The numerical verifications show that our proposed model provides an accurate and efficient solution method with the DOFs' economy.

The framework of this paper is as follows. Section 2 presents the FE formulations of the proposed elements in detail. The definitions of the related parameters are introduced, and then the basic stiffness equations of the new elements are deduced based on the minimum potential energy variational principle. A new element developed on the OpenSees computational framework based on the presented formulations is included in this section. Section 3 shows the validation of the proposed model for both concrete box girders and steel-concrete composite girders, under either the elastic or plastic loading states. Detailed comparisons are shown, including the results from the literature, tests, and the shell/solid refined FE model. Section 4 presents our concluding remarks about the applicability and effectiveness of the proposed model.

$$\psi(z)=\begin{cases}\left[1-\dfrac{(z+b_1+b_2)^2}{b_1^2}\right]\left(\dfrac{b_1}{b_2}\right)^2, & (y_k,z_k)\in\Omega_u\cap z_k\in(-b_1-b_2,-b_2)\\ 1-\dfrac{z^2}{b_2^2} & (y_k,z_k)\in\Omega_u\cap z_k\in(-b_2,b_2)\\ \left[1-\dfrac{(z-b_1-b_2)^2}{b_1^2}\right]\left(\dfrac{b_1}{b_2}\right)^2, & (y_k,z_k)\in\Omega_u\cap z_k\in(b_2,b_1+b_2)\\ 0 & (y_k,z_k)\notin\Omega_u\end{cases} \tag{1}$$

$$\chi(z)=\begin{cases}1\text{-}\dfrac{z^2}{b_2^2} & (y_k,z_k)\in\Omega_b\cap z_k\in(\text{-}b_2,b_2)\\ 0 & (y_k,z_k)\notin\Omega_b\end{cases} \tag{2}$$

2. FE formulations

2.1 Numerical simulation procedure

The model is built with assumptions and corresponding explanations are listed as follows:

(1) The mechanical behavior of girder is dominated by flexure, and the vertical shear deformation and shear failure are not considered.
(2) For composite girders, steel beams and RC slab are assumed to work compatibly through full shear connection and the slip effect is neglected.

Fig. 1 shows the geometry and notations of the proposed fiber beam element with the shear-lag effects. The x-axis of the element local coordinate system is established along with the longitudinal (i-j) direction. The y-axis and z-axis are built along with the height and transverse direction of the cross-section, respectively. The warping intensities f, g and the distribution shape functions $\psi(z)$, $\chi(z)$ account for the kinematic behavior of the shear lag of the reinforced concrete (RC) slabs. The element length is defined as L, and two nodes, named i and j, are located at opposite ends. Each node has five DOFs: axial displacement u, vertical displacement v, section angle θ, warping intensity f for the upper slab and warping intensity g for the lower slab. The cross-section of the element is described by a series of discrete fibers. Figs 1(a) and (b) show diagrammatic sketches of the fiber cross-section for a typical concrete box girder and the steel-concrete composite girders. The geometrical and material parameters of each fiber are specified, including the centroid coordinates of the fiber y_k, z_k, area of the fiber A_k, fiber elastic modulus E_k, and fiber shear modulus G_k. The values of the warping shape functions are calculated using the z coordinates of the fibers' centroid, and the physical meanings are the warping displacements with the unit warping intensity.

Following the suggestions presented in an earlier study (Gara *et al*. 2009) and we utilize quadratic polynomials to express the shape functions $\psi(z)$ and $\chi(z)$, as shown in Eqs. (1) and (2), in which b_1 and b_2 are the geometrical parameters of the flange (Fig. 1). Ω_u and Ω_b represent the regions where the warping of the upper and lower slabs will occur, respectively. If the centroid coordinates of fiber k (y_k, z_k) are not in the region Ω_u or Ω_b, this fiber would not appear to warp and the corresponding warping shape function values should be 0, i.e., $\psi(z_k) = 0$ or $\chi(z_k) = 0$. For cases where only 1 warping DOF exists in the element, as shown in Fig. 1(b), the shape function value of the other warping DOF should be 0.

2.2 Stiffness equations

According to the definition, the nodal displacements δ^e of this element can be expressed as a 10×1 vector, as shown in Eq. (3), in which the subscripts i and j represent the nodal numbers. The basic deformation vector δ_b^e without rigid body displacement is defined as Eq. (4). Then, the transformation relation between δ_b^e and δ^e is defined as Eq. (5). The deformation field inside the element can be interpolated by the basic displacement vector δ_b^e with the Hermite polynomial interpolation method. For a two-node element, the angular deformation $\theta(x)$ can be interpolated by a quadratic polynomial, and the axial deformation $du(x)$ and the warping intensities $f(x)$ and $g(x)$ can be interpolated by linear interpolation. The deformation field vector inside the element can be expressed as Eq. (6), in which $\xi = x/L$, x represents the local coordinates in the element, and $0 \le \xi \le 1$.

As shown in Fig. 2, the longitudinal deformation at any location in the element can be obtained by the superposition of four components: the axial deformation, bending deformation, and warping deformation of the upper and lower slabs, as expressed in Eq. (7).

Based on the Euler-Bernoulli beam theory, the vertical (y-direction) shear deformation is ignored, i.e., $\gamma_{yz} = \gamma_{xy} = 0$. The non-vanishing strain can be expressed as Eq. (8) by a geometric equation, in which $\varepsilon(x, y, z)$ is the axial strain along the length of the element; $\gamma_{xz}(x, y, z)$ is the shear strain of the concrete slab in the xOz plane; and $\psi_{,z}(z)$ and $\chi_{,z}(z)$ denote the partial derivative of the warping shape functions $\psi(z)$ and $\chi(z)$ with respect to the z coordinate, respectively.

The stress vector in the element is expressed as $\mathbf{s}(x, y, z) = [\sigma(x, y, z)\ \ \tau(x, y, z)]^T$, in which $\sigma(x, y, z)$ represents the normal stress at a specified position and $\tau(x, y, z)$ represents the shear stress in the xOz plane. With the specified strain, the stress vector $\mathbf{s}(x, y, z)$ can be obtained from the material constitutive equation.

$$\boldsymbol{\delta}^e = \begin{bmatrix} u_i & v_i & \theta_i & f_i & g_i & u_j & v_j & \theta_j & f_j & g_j \end{bmatrix}^T \tag{3}$$

$$\boldsymbol{\delta}_b^e = \begin{bmatrix} du & \theta_i' & \theta_j' & f_i & g_i & f_j & g_j \end{bmatrix}^T \tag{4}$$

$$\boldsymbol{\delta}_b^e = \begin{bmatrix} -1 & 0 & 0 & 0 & 0 & 1 & 0 & 0 & 0 & 0 \\ 0 & \frac{1}{L} & 1 & 0 & 0 & 0 & \frac{-1}{L} & 0 & 0 & 0 \\ 0 & \frac{1}{L} & 0 & 0 & 0 & 0 & \frac{-1}{L} & 1 & 0 & 0 \\ 0 & 0 & 0 & 1 & 0 & 0 & 0 & 0 & 0 & 0 \\ 0 & 0 & 0 & 0 & 1 & 0 & 0 & 0 & 0 & 0 \\ 0 & 0 & 0 & 0 & 0 & 0 & 0 & 0 & 1 & 0 \\ 0 & 0 & 0 & 0 & 0 & 0 & 0 & 0 & 0 & 1 \end{bmatrix} \boldsymbol{\delta}^e = \mathbf{P}\boldsymbol{\delta}^e \tag{5}$$

$$\begin{aligned} \boldsymbol{\delta}_b(x) &= \begin{bmatrix} du(x) & \theta(x) & f(x) & g(x) \end{bmatrix}^T \\ &= \begin{bmatrix} \xi & 0 & 0 & 0 & 0 & 0 & 0 \\ 0 & 3\xi^2-4\xi+1 & 3\xi^2-2\xi & 0 & 0 & 0 & 0 \\ 0 & 0 & 0 & 1-\xi & 0 & \xi & 0 \\ 0 & 0 & 0 & 0 & 1-\xi & 0 & \xi \end{bmatrix} \boldsymbol{\delta}_b^e \\ &= \mathbf{N}(x)\boldsymbol{\delta}_b^e \end{aligned} \tag{6}$$

$$u(x, y, z) = \begin{bmatrix} 1 & -y & \psi(z) & \chi(z) \end{bmatrix} \boldsymbol{\delta}_b(x) \tag{7}$$

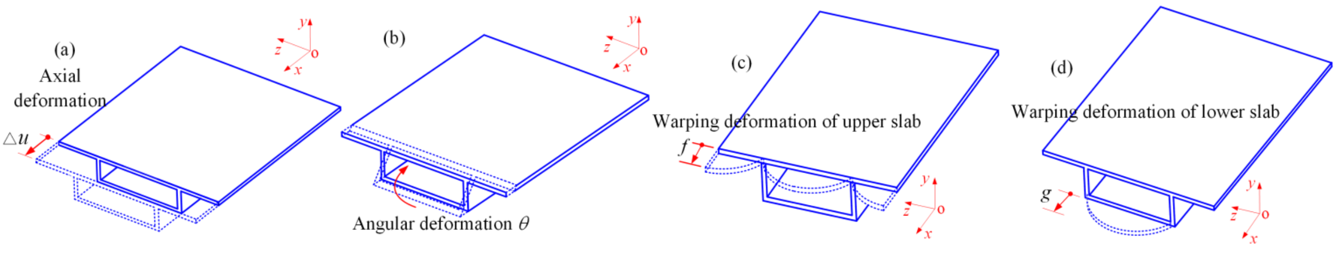

Fig. 2 Components of the longitudinal deformation in the element: (a) axial deformation; (b) angular deformation; (c) warping deformation of the upper slab; (d) warping deformation of the lower slab

$$\boldsymbol{\eta}(x,y,z)=\left[\varepsilon(x,y,z)\quad \gamma_{xz}(x,y,z)\right]^T=\mathbf{Q}(y,z)\mathbf{B}(x)\boldsymbol{\delta}_b^e$$

$$=\begin{bmatrix}1 & -y & \psi(z) & \chi(z) & 0 & 0\\ 0 & 0 & 0 & 0 & \psi_{,z}(z) & \chi_{,z}(z)\end{bmatrix}\begin{bmatrix}\frac{1}{L} & 0 & 0 & 0 & 0 & 0 & 0\\ 0 & \frac{6\xi-4}{L} & \frac{6\xi-2}{L} & 0 & 0 & 0 & 0\\ 0 & 0 & 0 & \frac{-1}{L} & 0 & \frac{1}{L} & 0\\ 0 & 0 & 0 & 0 & \frac{-1}{L} & 0 & \frac{1}{L}\\ 0 & 0 & 0 & 1\text{-}\xi & 0 & \xi & 0\\ 0 & 0 & 0 & 0 & 1\text{-}\xi & 0 & \xi\end{bmatrix}\boldsymbol{\delta}_b^e \tag{8}$$

As the displacement δ^e occurs, the potential energy of the element can be expressed as

$$\Pi^e=\frac{1}{2}\int_\Omega \mathbf{s}(x,y,z)^T\boldsymbol{\eta}(x,y,z)-\mathbf{F}^{eT}\boldsymbol{\delta}^e,$$

in which $\mathbf{F}^{eT}$ is the external load applied to the element, which can be obtained by integrating the product of load density and displacement shape function along the element length, as illustrated by the classical FE theory (Bathe 2014). The stiffness equation of the element can be deduced by the variational of the potential energy.

The tangent stiffness matrix $\mathbf{K}^e$ of the element can be deduced as

$$\mathbf{K}^e=\mathbf{P}^T\cdot\int_l \mathbf{B}^T(x)\cdot\mathbf{k}^s\cdot\mathbf{B}(x)\cdot dx\cdot\mathbf{P} \tag{9}$$

in which $\mathbf{k}^s$ denotes the section tangent stiffness matrix.

In addition, the element resisting force vector is needed to determine the convergence, as shown in Eq. (10), in which $\mathbf{r}^s$ denotes the section resisting force vector.

$$\mathbf{R}^e=\mathbf{P}^T\cdot\int_l \mathbf{B}^T(x)\cdot\mathbf{r}^s\cdot dx \tag{10}$$

For the fiber beam element, integrations of the section resisting force vector and stiffness matrix can be viewed as the algebraic sum of various fibers' contributions, as shown in Eqs. (11) and (12), respectively. In which, n is the total number of fibers in the section; E_k and σ_k are the tangent modulus and normal stress of the kth fiber, respectively; G_k and τ_k are the shear modulus and shear stress, respectively. By the definitions of the different fibers, the proposed model can be applied to structures with different types of cross-sections. The fiber stiffness can be updated with respect to the change of the stress states during the elastoplastic iterative process. The components in the section resisting force vector represent the axial force, bending moment, axial forces induced by the warping of the two slabs, and shear forces induced by the warping of the two slabs.

$$\mathbf{r}^s=\sum_{k=1}^{n}\left[\sigma_k A_k\quad -\sigma_k A_k y_k\quad \sigma_k A_k\psi(z_k)\quad \sigma_k A_k\chi(z_k)\quad \tau_k A_k\psi_{,z}(z_k)\quad \tau_k A_k\chi_{,z}(z_k)\right]^T \tag{11}$$

$$\mathbf{k}^s=\sum_{k=1}^{n}\begin{bmatrix}E_kA_k & -E_kA_ky_k & E_kA_k\psi(z_k) & E_kA_k\chi(z_k) & 0 & 0\\ & E_kA_ky_k^2 & -E_kA_ky_k\psi(z_k) & -E_kA_ky_k\chi(z_k) & 0 & 0\\ & & E_kA_k\psi^2(z_k) & E_kA_k\psi(z_k)\chi(z_k) & 0 & 0\\ & & & E_kA_k\chi^2(z_k) & 0 & 0\\ & sym & & & G_kA_k\psi_{,z}^2(z_k) & G_kA_k\psi_{,z}(z_k)\chi_{,z}(z_k)\\ & & & & & G_kA_k\chi_{,z}^2(z_k)\end{bmatrix} \tag{12}$$

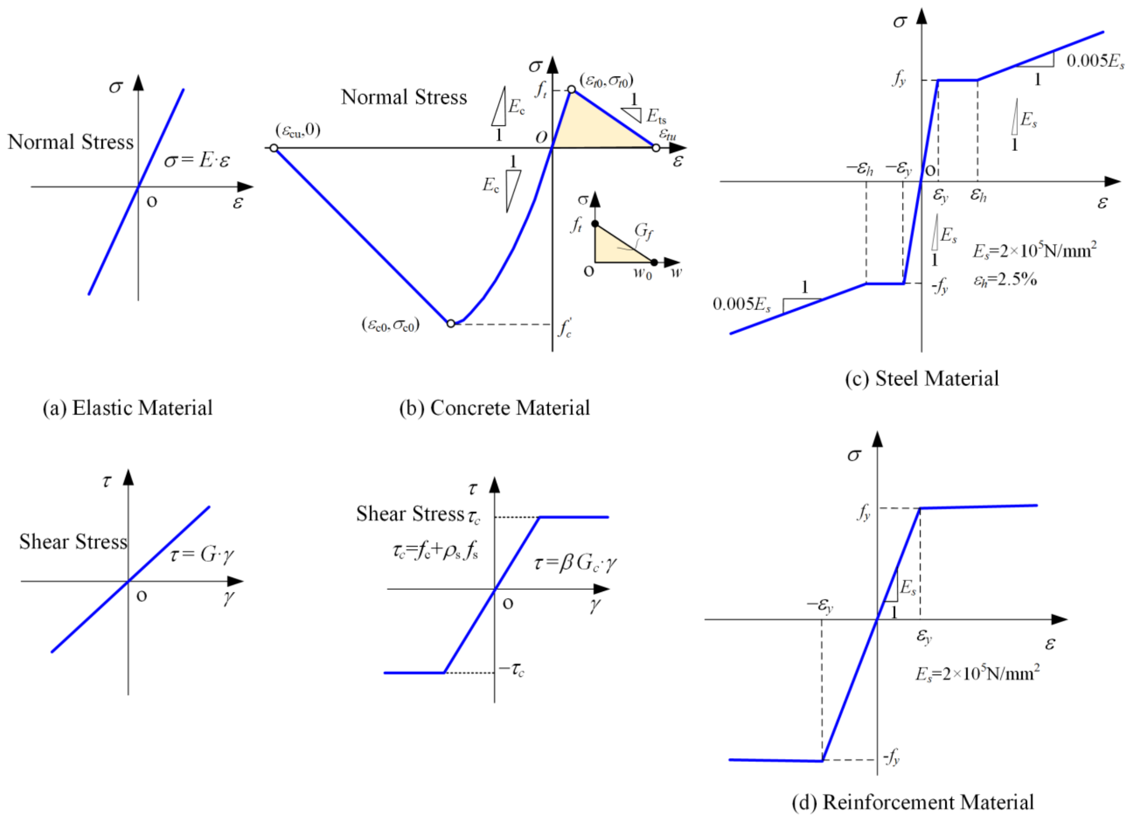

Fig. 3 Uniaxial constitutive relationships for materials

The element stiffness matrix and resisting force vector can be calculated by the Gauss-Lobatto integration method, with the ones of the sections at the integral points. The structural analysis can be conducted after the assembly. The size of the structural stiffness matrix is greatly reduced because the sectional warping is described by only two introduced DOFs, and the computational cost consequently decreases.

The formulation is developed in a two-dimensional system, without conceptual difficulty in three dimensions. It should be noted that this model is also applicable to structures with only one warping DOF, as shown in Fig. 1(b), which only needs to constrain the redundant warping DOF of the element. Similarly, if all the shear-lag warping DOFs were constrained, this model degenerates to the conventional fiber beam element.

2.3 Constitutive relations

The constitutive equations of four commonly adopted materials are considered in this study: the elastic material, concrete material, steel material, and reinforcement material.

(1) Elastic material

Elastic material was used to analyze the elastic shear-lag effect of structures. For the elastic material, the constitutive relations between the normal stress-strain and shear stress-strain all satisfy Hooke's law, as shown in Fig. 3(a).

(2) Concrete material

Fig. 3(b) shows the uniaxial stress-strain curve of the concrete. The compressive stress-strain relationship is assumed in the parabolic-ascending linear-descending form proposed by Hognestad *et al.* (1955), as stated in Eq. (13). ε_{c0} is the peak compressive strain; the peak compressive stress σ_{c0} equals the cylinder concrete compressive strength $f_c^{'}$. The concrete softening stiffness is determined by the data point (ε_{cu}, 0). To mitigate the mesh sensitivity problems, ε_{cu} is set as a mesh adjusted strain, specified by characteristic length of the respective FE integration point and volume specific localized crushing energy (Wendner *et al.* 2015). The initial tangent modulus of concrete E_c = $2\sigma_{c0}/\varepsilon_{c0}$.

The tension stress-strain relationship is shown in Eq. (14), and the curve is shown in Fig. 3(b). The peak tensile stress $\sigma_{t0} = f_t$, in which f_t is the concrete tensile strength; the peak tensile strain $\varepsilon_{t0} = f_t/E_c$. The smeared crack model is employed to simulate the tensile softening behavior of concrete after cracking. According to the crack band theory, the ultimate tensile strain ε_{tu} can be determined with the concrete fracture energy G_f, which is provided in CEB-FIP (2010). The tension softening stiffness E_{ts} can be expressed as $E_{ts} = \sigma_{t0}/(\varepsilon_{tu}-\varepsilon_{t0})$.

Unlike the constitutive relation in the normal direction, the shear constitutive model in concrete is complicated due to the aggregate interlocking effect, dowel action, and contribution of the hoop reinforcements. A non-linear elastic relation, as shown in Fig. 3(b) is adopted for

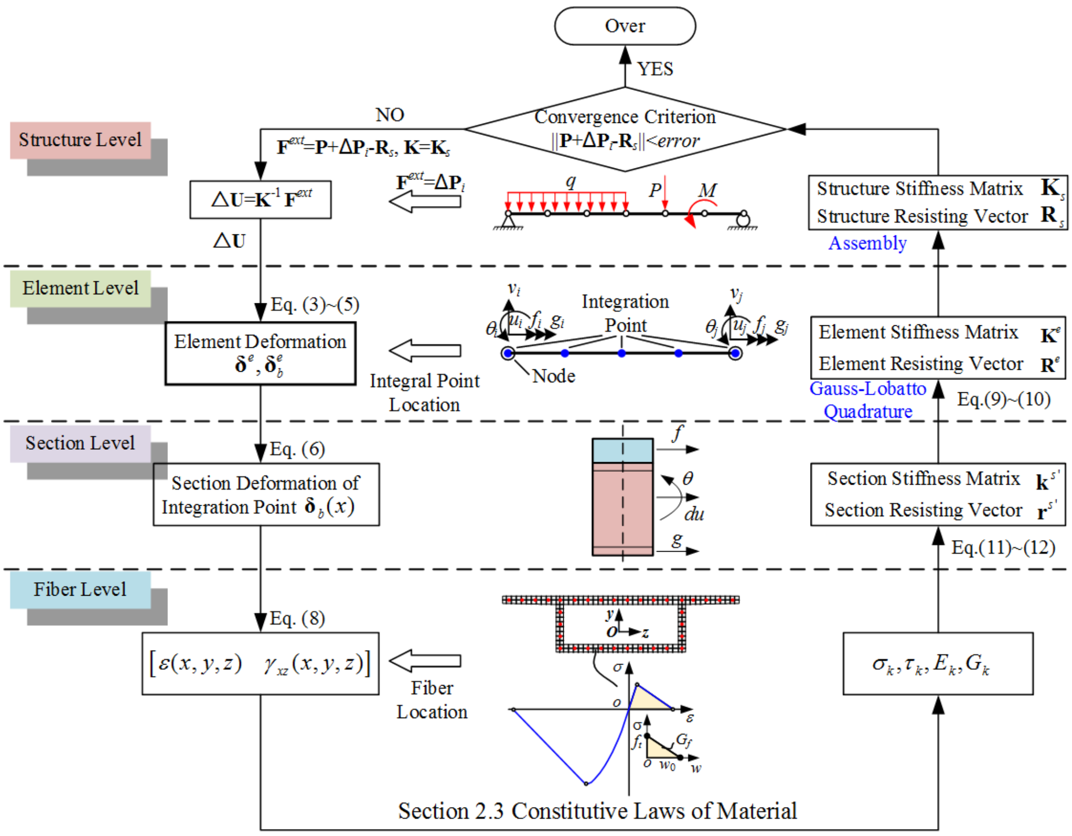

Fig. 4 Flow chart of the iterative computation process

concrete shear constitutive relation for that enough stirrups are usually arranged in practice to prevent the shear failure. τ_c is the maximum shear stress, as shown in Fig. 3(b), in which f_c denotes the concrete tensile strength, ρ_s and f_s denote the reinforcement ratio and strength of stirrup respectively. The shear modulus G_c was calculated as $G_c = E_c/2/(1+\nu_c)$, in which ν_c is Poisson's ratio of concrete, which generally has a value of 0.2. As concrete cracked, G_c was multiplied by a shear retention factor β = 0.5 to consider diminished shear stiffness.

$$\sigma=\begin{cases}\sigma_{c0}\left[2\left(\dfrac{\varepsilon}{\varepsilon_{c0}}\right)-\left(\dfrac{\varepsilon}{\varepsilon_{c0}}\right)^2\right], & \varepsilon_{c0}\le\varepsilon\le 0\\ \sigma_{c0}\left[1-\left(\dfrac{\varepsilon\text{-}\varepsilon_{c0}}{\varepsilon_{cu}-\varepsilon_{c0}}\right)\right], & \varepsilon\le\varepsilon_{c0}\end{cases} \tag{13}$$

$$\sigma=\begin{cases}E_c\cdot\varepsilon, & 0\le\varepsilon\le\varepsilon_{t0}\\ \sigma_{t0}-E_{ts}(\varepsilon-\varepsilon_{t0}), & \varepsilon_{t0}\le\varepsilon\le\varepsilon_{tu}\end{cases} \tag{14}$$

(3) Steel and reinforcement material

The trilinear model with a yield plateau is adopted for the steel material, as shown in Fig. 3(c). E_s is the initial tangent modulus; the hardening modulus is $0.005E_s$; ε_h denotes the hardening strain generally valued 0.025. The elastic-perfectly plastic model is adopted for the reinforcement material, as shown in Fig. 3(d). The reinforcement fiber shear stiffness does not contribute to the ection stiffness in Eq. (12), i.e., the shear modulus of the reinforcement material is 0.

2.4 Numerical simulation procedure

For flexibility, extensibility, and portability, we developed the proposed model on the computational framework of OpenSees software (Gandelli *et al*. 2019), as a new derived Element class. The interpreter codes for the corresponding *Tcl* command were also developed. The full Newton iteration method was used to solve the structural non-linearity equations. In every iteration step, the stiffness and stresses of fibers were updated according to the different stress states. The stiffness matrices and resisting force vectors of the section level, element level, and structure level were updated in turn (Fig. 4).

3. Case study

To verify the validity of our theoretical model, the proposed model and the newly developed element were applied to some representative cases under the elastic or plastic loading states and compared with the solutions of existing theoretical models, tests, and the shell/brick refined FE model.

3.1 Elastic shear-lag analysis

(1) Simply supported box girder

Luo *et al*. (2002b) tested the elastic shear-lag effect of scaled plexi-glass simply supported box girder. The cross-section is shown in Fig. 5(a). The span is 800 mm, and the concentrated load P = 272.2 N is applied at the mid-span. The elastic modulus E = 3000 MPa, and the shear modulus G = 1083 MPa. Zhou (2010) presented the theoretical solution of the specimen based on the suggested model.

A model containing 40 proposed elements is established according to the dimensions and material parameters of the specimen. The plexi-glass is simulated as elastic material reasonably due to that the stress level of the specimen is far below plastic stress during the tests (Luo *et al*. 2002b). The cross-section is discretized into a series of fibers with an approximate size of 5 mm. The analysis results are compared with the test data and Zhou's method (Zhou 2010).

Fig. 5(b) shows the deformation curve of the simply supported beam under concentrated loading at the mid-span, and the results of the proposed model are consistent with those of Zhou (2010), but the elementary beam theory overestimates the beam stiffness. Fig. 5(c) shows the transverse distribution of the normal stress on the upper and lower slabs at the mid-span section, and the shear-lag effect is significant. The calculated stresses of the proposed model show a high accuracy compared with the results of tests and Zhou's study. To discuss the sensitivity of the element number, we create models by varying the mesh of the beam's longitudinal axis. The deflection results of the 2, 4, 6, 8, and 10 element models are shown in Fig. 5(b). The comparisons show that the results tend to converge with the increasing element number, and good accuracy is obtained with more than 10 elements in the case of the mid-span point load.

As defined by Zhou (2010), the shear-lag effect coefficient λ is introduced as $\lambda = \sigma_x/\bar{\sigma}_x$ to quantify the influence of the shear-lag effects on stress, in which σ_x is the stress of the proposed model with the shear-lag effects and $\bar{\sigma}_x$ is the stress based on the elementary beam theory following the assumption of a planar cross-section. Figs. 5(d) and (e) show the longitudinal distribution of λ along the girder under concentrated load and uniformly distributed load respectively. The results show that the shear-lag effect coefficient is affected by the loading type. The shear lag effect at the end of simply supported beams is lower than mid-span section under concentrated load, while reverse under uniformly distributed load. The same results were obtained by Zhou (2010).

(2) Continuous box girder

Fig. 6 shows the results of an experimental study on the elastic shear-lag effect of a 3-span variable-height continuous box girder conducted by Luo *et al*. (2002a). The span arrangement of this girder is 460 mm + 860 mm + 460 mm, and the height varies in a quadratic parabolic form, being 80 mm at the 2 internal supports and 40 mm at the middle of the main span. The specimen was made of plexi-glass, whose Young's modulus is E = 2,600 MPa and the Poisson's ratio ν = 0.4. A vertical uniformly-distributed load q = 0.5 kN/m was applied to the whole structure. Zhang and Lin (2014) proposed a model with an additional deflection as the generalized displacement for analysis of this test.

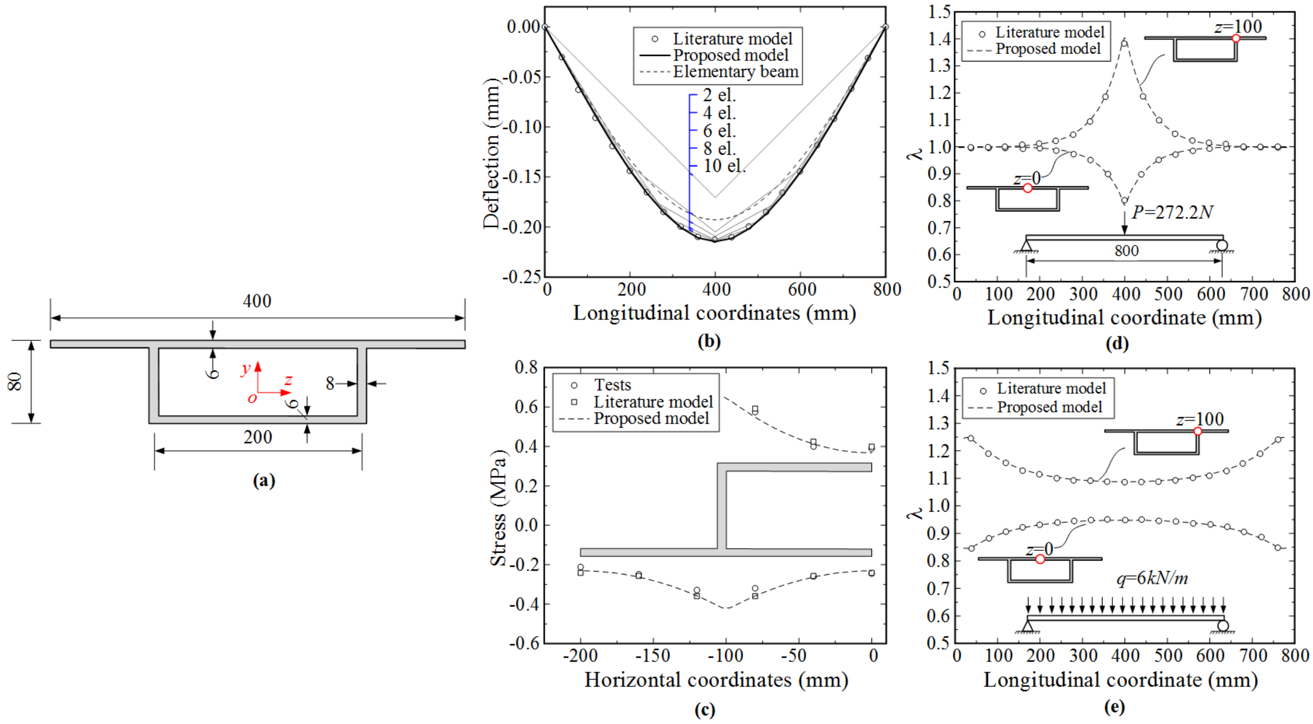

Fig. 5 Elastic shear-lag effect analysis for the simply supported box girder: (a) cross-section of the box girder (unit: mm); (b) structural deflections; (c) transverse distribution of the normal stress on the upper and lower slabs at the mid-span section; (d) shear-lag coefficient under a concentrated load ; (e) shear-lag coefficient under uniformly distributed load

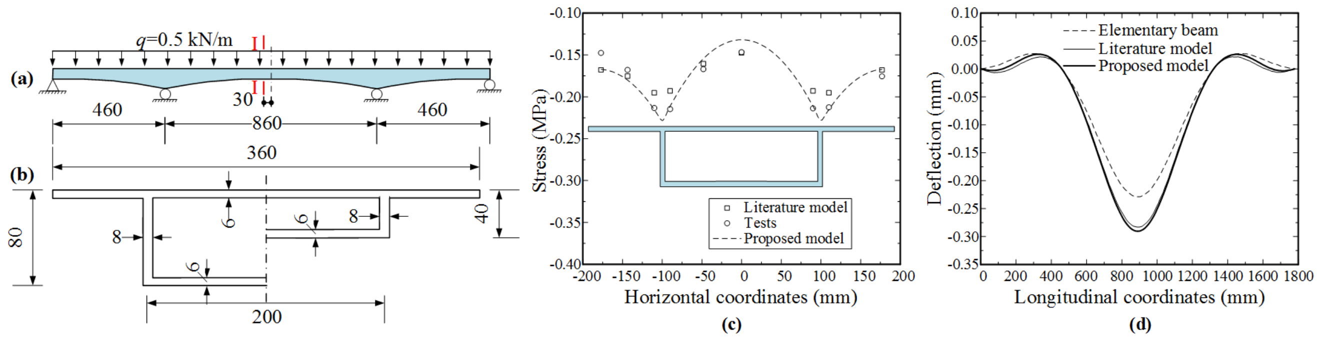

Fig. 6 Elastic shear-lag effect analysis for the continuous box girder (unit: mm): (a) span arrangement and typical cross-section; (b) cross-sections; (c) transverse distribution of normal stress at section I-I; (d) structural deflection

The proposed model is also applied to the test. The model is discretized into 178 elements, and the geometric properties of the cross-section of each element are chosen to be the average values of those at the two ends. The mesh size of the sectional discrete fibers is 6 mm, and the plexiglass is simulated as elastic material for the same reason with simply supported box girder case. Fig. 6(c) shows the transverse distribution of the normal stress at section I-I, and the results reveal that a significant shear-lag effect on the upper slab can be observed. The results of the proposed model are close to the theoretical results found by Zhang and Lin (2014) and the test performed by Luo *et al*. (2002a) on the whole. Due to some test deviation, some variances are observed at flange away from the web. Fig. 6(d) shows the structural deflection curve, and the comparisons indicate the applicability of the proposed model for a continuous box girder. We concluded that the elementary beam model underestimates approximately 30% of the deflection if the shear-lag effect is ignored, which proves that it is necessary to consider the shear-lag effect in structural analysis.

(3) Steel-concrete composite girder

A practical two-span steel-composite bridge is employed to verify the applicability of the proposed model to a steel-concrete composite girder (Fig. 7). The cross-section parameters are shown in Fig. 7(a). The span arrangement and the boundary conditions are shown in Fig. 7(b). There were two lanes on the bridge, and the traffic live load (uniform load 10.5kN/m and concentrated load 330 kN for each lane) specified in Chinese code (JTG D60-2015) are

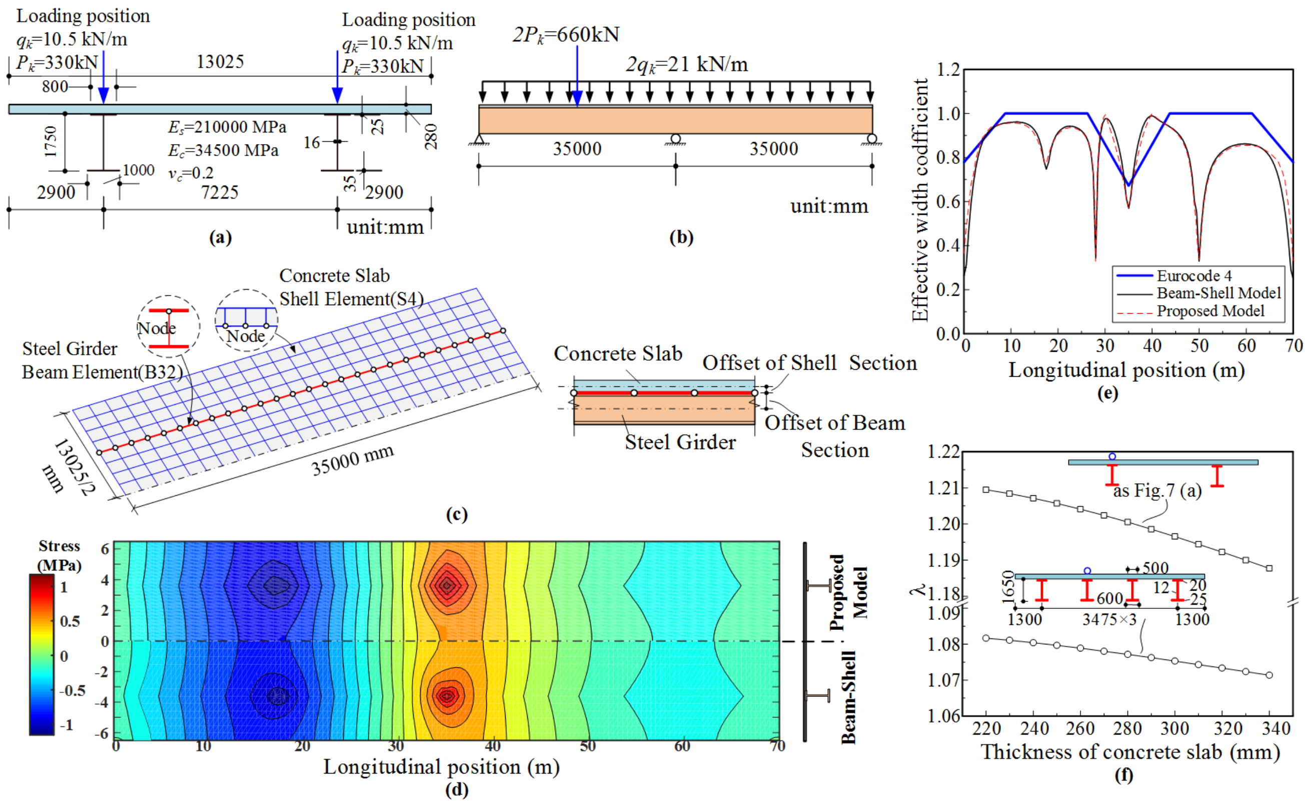

Fig. 7 Elastic shear-lag effect analysis for the steel-concrete composite girder:(a) cross-section (unit: mm); (b) load type; (c) beam-shell hybrid model; (d) contour plot of the normal stress of the concrete slab; (e) effective width coefficient of concrete slab; (f) shear-lag coefficient with varying slab thickness (unit: mm)

applied to the bridge, as shown in Fig. 7. A fiber beam element model with 70 elements is built. The concrete slab was discretized as 100 fibers with a layout of 1 row and 100 columns.

For verification, a refined analysis model based on the beam and shell elements is also created in *ABAQUS 6.14* software (ABAQUS 2014). Fig. 7(c) illustrates the method for this refined analytical model, in which the concrete slab is simulated by the integral shell element (S4) and the steel girder is simulated by the Euler beam element (B32). Both the beam and shell element are modeled in the same plane with share-node method as shown in Fig. 7(c). The eccentricity of the sections is set to consider the offset between the center of sections and the location of nodes for both two types of element. The element stiffness is determined on the axis after eccentricity. The modeling approach of this refined model has been verified in several studies (Nie *et al*. 2011, Nie and Tao 2012).

The normal stresses at the mid-surface of the concrete slab are extracted from the results of the refined model and the fiber beam model. The contour plot of the normal stress shown in Fig. 7(d) shows that the results of the fiber beam model are very close to those of the refined model throughout the entire slab region.

The effective width coefficient $\beta = b_{\rm eff}/b$ is always adopted to evaluate the shear-lag effects, in which $b_{\rm eff}$ and b denote the effective and actual slab width respectively. Based on the definition of Zhu *et al*. (2015), the effective width coefficient of concrete slab was calculated with the two models and the suggested formula specified in Eurocode 4 (2004) was also presented for comparisons, as shown in Fig. 7(e). The results show that the proposed model has a good agreement with the refined model while the Eurocode 4 method shows some deviations.

Fig. 7(f) reports the effect of slab thickness on the shear-lag coefficient at mid-span. Another practical bridge with the same width and span but 2 more steel girders (section dimensions shown in Fig. 7(f)) was also analyzed to make a comparison. The shear-lag coefficient increase with the decreasing slab thickness and number of steel girders.

3.2 Elastic-plastic shear-lag analysis

(1) RC box girder

Cao and Fang (2016) carried out an experimental study on the cracking process of a two-span RC continuous box girder under uniform load. The span arrangement of this girder was 4.425 m + 4.425 m. A uniform load q = 116.8 N/m was loaded on the specimen in a stepwise manner. The cross-section is shown in Fig. 8(a).

The proposed model and traditional fiber beam element model based on elementary beam theory were used to establish the numerical model for comparison. Fig. 8(b) shows the load-deflection curve at the mid-span. The elementary beam theory overestimates the initial tangent stiffness and cracked stiffness, and the proposed model is in good agreement with the experimental results.

Fig. 8(c) presents the curves of the maximum tensile

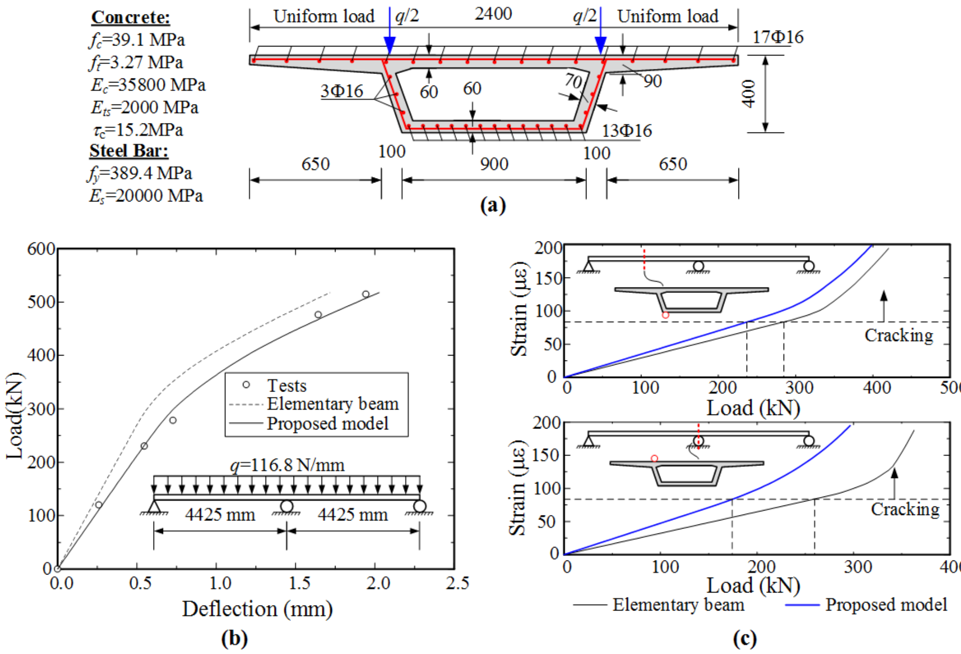

Fig. 8 Elastoplastic analysis of the RC box girder: (a) cross-section (unit: mm); (b) load-deflection curves; (c) cracking loads of the upper and lower slabs

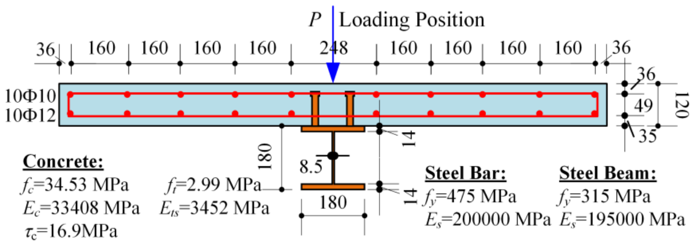

Fig. 9 Sectional dimensions and material for the B-4 specimen

strain of the lower and upper concrete slabs as the load increases. The cracking loads of the two models were obtained with the cracking criterion of peak tensile strain. The results show that with increasing load, the girder cracks start from the upper slab of the mid-support section, which causes moment redistribution. Then cracks occur on the lower slab at the mid-span section, which causes bi-linear load-deflection curves at mid-span. Compared with the proposed model, the elementary beam model overestimates the cracking load on both sections, which indicates the necessity of considering the shear-lag effect during the analysis of a box girder with a wide flange.

(2) Steel-concrete composite girders subjected to the sagging bending moment

The mechanical behavior of steel-concrete composite girders under elastic-plastic loading states was studied by Amadio *et al.* (2004). Fig. 9 shows the sectional dimensions and material of the test girder subjected to the sagging bending moment, which is named B-4 in the literature (Amadio *et al.* 2004). The B-4 specimen was a simply supported girder with a 3800 mm span, and two vertical concentrated loads 1 m apart are applied in symmetric positions with respect to the mid-span, as shown in Fig. 10.

A proposed model containing 76 elements is built to analyze the elastic-plastic behavior of the B-4 specimen up to collapse. The concrete slab section is divided into 250 fibers, with five divisions along with the height and 50 divisions along the width. The steel girder is divided into 20 fibers along the height direction, and the longitudinal reinforcements are inserted as rebar fibers. For verification, a fine beam-shell element model, as presented in Section 3.1, is also built with *ABAQUS 6.14* to conduct the non-linear analysis. In the beam-shell model, the rebar layers are inserted into the shell element based on the area equivalence principle to evaluate the contribution of reinforcement to the compressive behavior of the concrete slabs (ABAQUS 2014). The Concrete Damaged Plasticity (CDP) material model is adopted in the beam-shell model to simulate the non-linear behavior of concrete, and the reinforcements and steel beams are simulated by the isotropic hardening plastic material model. The uniaxial constitutive relationships among concrete, steel beams, and steel bars for both models are consistent with those presented in Section 2.3.

Fig. 10 shows the load-deflection curves (mid-span deflection) and the deviations of two numerical models. The proposed model agrees well with the beam-shell model with

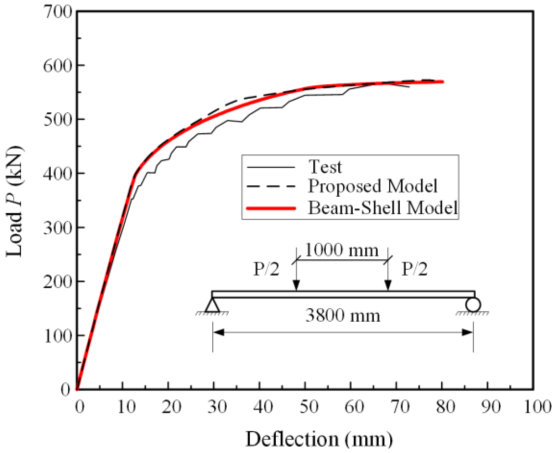

Displacement (mm)	Deviations of Load (%)	
	$\lvert P_p\text{-}P_t\rvert/P_t$	$\lvert P_p\text{-}P_{bs}\rvert/P_{bs}$
10	8.45	0.14
20	9.23	0.68
30	7.23	1.71
40	5.06	1.43
50	2.52	0.18
60	1.72	0.19
65	0.89	0.05

P_{pk}: load result of proposed model
P_t: load result of test
P_{bs}: load result of Beam-Shell model

Fig. 10 Load-deflection curves for the B-4 girder

deviations less than 1.71%, especially in terms of the initial stiffness and ultimate bearing capacity of the girder. Compared with the experimental results, the analysis results are close on the whole with deviations less than 9.23%. The deviations are acceptable for the material variance may be existed due to initial imperfection.

Fig. 11 shows the stress contour plot of the upper concrete slab under various loading stages. With the increasing load, the plastic deformation of the concrete slab develops, and the stress distribution in the pure bending section of the span gradually becomes uniform, that is, the stress lag effect decreases. The stress distribution of the proposed model is close to that of the beam-shell model, under both the elastic and elastoplastic loading states.

Due to the compression soften effect after the concrete peak compressive strain reached, the adjacent fibers (such as from 0 to 1400 mm in Fig. 11) near the crushing region would unload. In the Beam-shell model, the unloading process occurred locally and gradually. While in the proposed model, the process is coinstantaneous and slower than the refined model for that only one DOF is employed to describe the warping deformation for high efficient analysis. As shown in Figs. 11(c) and (d), the unloading phenomena can be observed in both models. Even though some deviations exist in shear span for two models, well agreement can be observed in pure bending sections which need specifically concerned. The proposed model is applicable for analyzing the stress distribution of concrete slabs up to the compression failure.

(3) Steel-concrete composite girders subjected to the hogging bending moment

Fig. 12 shows another specimen, named B-1 in the literature (Amadio *et al*. 2004). It is a simply supported composite girder subjected to a hogging bending moment. The span is 3800 mm, and a vertical upward load is applied at the mid-span. Figs. 12(a) and (b) show the structural dimensions and material parameters.

The fiber beam model was built with the method used in the example for B-4 presented above, while the shell-solid

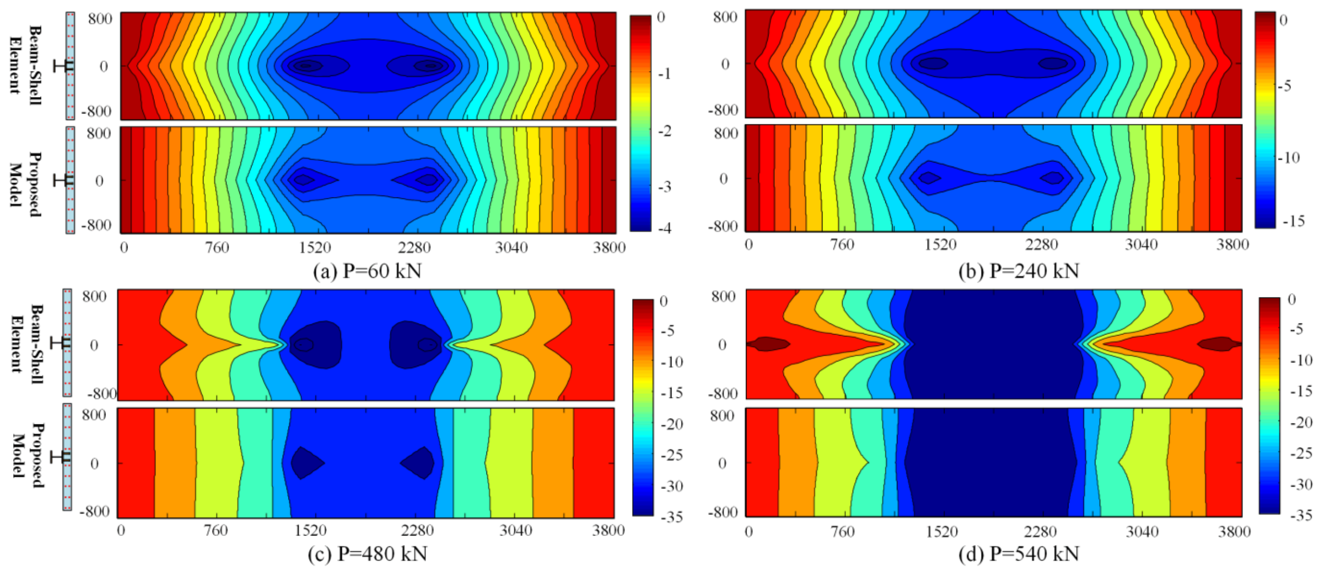

Fig. 11 Stress contour plot of the upper concrete slab under various loading stages

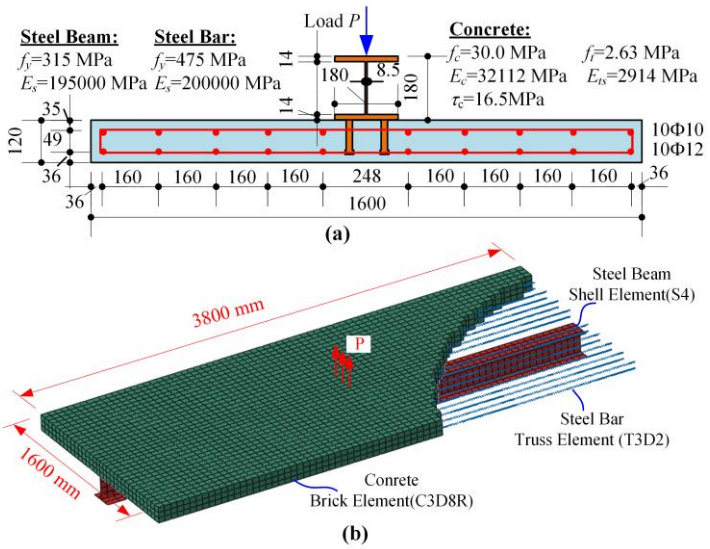

Fig. 12 Dimensions and analysis model for the B-1 specimen

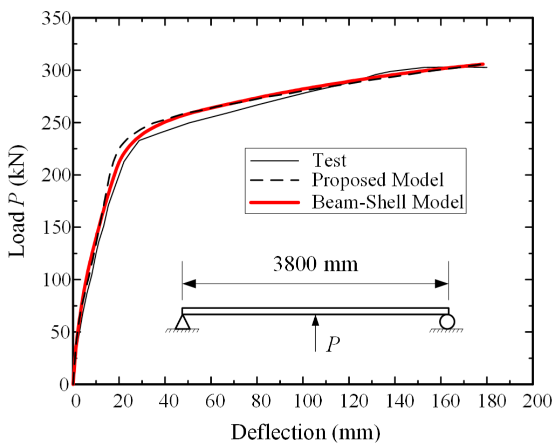

Displacement (mm)	Deviations of Load (%)	
	$\lvert P_p\text{-}P_t\rvert/P_t$	$\lvert P_p\text{-}P_{bs}\rvert/P_{bs}$
2.5	11.3	0.97
20	12.6	5.35
60	3.40	0.01
100	0.88	0.56
140	1.84	0.65
170	0.06	0.18

P_{pk}: load result of proposed model
P_t: load result of test
P_{bs}: load result of Beam-Shell model

Fig. 13 Load-deflection curves at the mid-span of the B-1 specimen

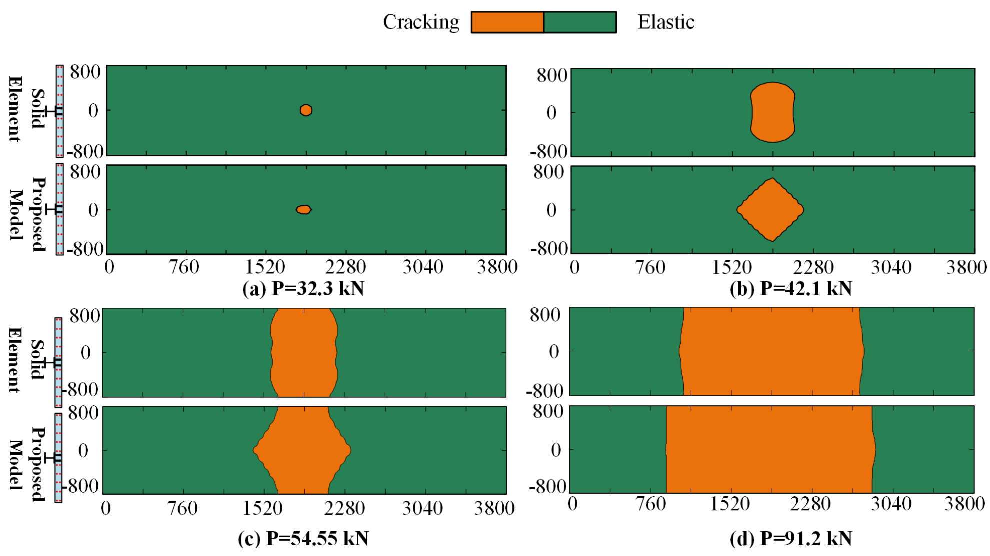

Fig. 14 Cracking regions of the concrete slab under various loading stages

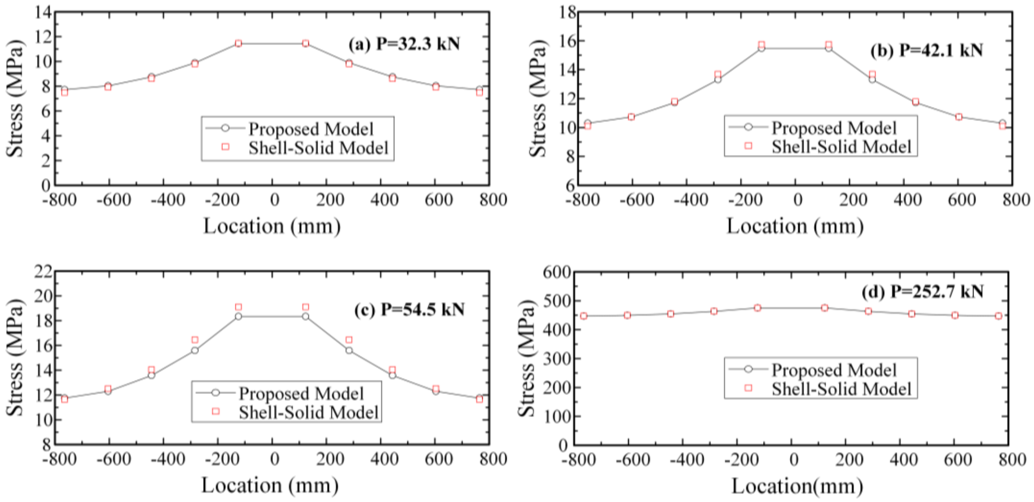

Fig. 15 Stress distribution of the reinforcements in the concrete slab under various loading levels

model was set up with *ABAQUS 6.14* to conduct the refined analysis for the comparisons. In the refined model, an 8-node reduced integral solid element (C3D8R) was used to simulate the concrete slab, a 4-node fully integrated shell element (S4) was used to simulate the steel girder, and a 2-node linear bar element (T3D2) was used to simulate the steel bar. The steel bar was coupled with the adjacent nodes of the concrete elements using the **embedded* method provided in *ABAQUS 6.14*, and the **tie* method in *ABAQUS 6.14* was used to model the rigid connection between the concrete slab and steel girder (ABAQUS 2014). The slip effect was ignored in the models.

Fig. 13 reports the load-deflection curves (mid-span deflection) and deviations of two numerical models. Well agreement is observed between the proposed model and the refined model with max deviations of 5.35%. Some deviations (within 12.6%) between the proposed model and tests exist and the reason is that local buckling behavior of steel beam occurred in the experiment while it is not considered in this study.

The fibers' tensile strain of the upper concrete slab was extracted from the shell-solid model and the proposed model. Taken the peak tensile strain as the cracking criterion, the cracking regions under various load levels for the two models are plotted, as shown in Fig. 14. Because of the shear-lag effect, the concrete slab cracks at the center of the mid-span section firstly; then, the cracking regions develop throughout the entire slab width with the increasing load. The comparisons between the two models show that the proposed model is relatively accurate for predicting both the cracking load and the evolution of the cracking regions.

Fig. 15 shows the stress distribution of the 10ϕ12 steel bars in the concrete slabs under various loading levels. It shows that the results of the two analysis models are almost identical at the initial cracking stage (as shown in Fig. 15 (a)-(b)) and the stress distribution shows a "bell-like" shape. With the development of the plastic deformations (as shown in Fig. 15(c)), the stresses show a slight difference but have the same increasing trend. The reason can be explained as that less degree of freedom is employed to consider the warping deformation leading to the slower plastic development compared with the refined model. While with the plastic further development, the results show good agreement again under the load close to collapse (Fig. 15(d)).

4. Conclusions

A 10-DOF fiber beam element model considering the shear-lag effect and material non-linear behaviors is proposed for the elastic-plastic analysis of wide flange girders. The FE formulations and the computational procedure are presented. Several case studies under elastic and plastic loading states are analyzed. The effectiveness is verified by comparison with existing theoretical models, test results, and shell/solid element models. The main conclusions of our work are as follows:

- The case analysis results reveal that the shear-lag effect has a significant effect on the structural stiffness and stress distributions; the shear-lag effect cannot be neglected, particularly for wide flanged structures.
- Discrete fibers are employed in the proposed model to define the cross-section, which makes it applicable for structures with different types of cross-sections, such as concrete box girders and steel-concrete composite girders.
- The typical material non-linear behaviors are considered in the proposed model, like concrete cracking, crushing, and plastic deformation of steel bars and steel beams. A good agreement with the shell/solid refined element model is observed under the elastic and plastic hardening stage. Despite of some deviations under the plastic softening stage, the proposed model provides a high-efficient way to analyze the elastoplastic behavior of girders with shear lag effect. Especially for the calculation of initial stiffness and ultimate bearing capacity, this paper provides a unified analytical model.
- The proposed model and the developed OpenSees

program simplified the modeling process and improved analysis efficiency. The proposed model ran for less than 1 or 2 s for the elastic shear-lag analysis and less than 1 min for the elastoplastic analysis with an Intel Core i7 CPU @ 2.50 GHz processor. For the shell/solid FE model in ABAQUS 6.14, the time costs were typically 1-2 min and 1-2 h, respectively.

Acknowledgments

The authors would like to acknowledge the following financial supports to carry out the research: the Fundamental Research Funds for the Central Universities under Grant Nos. 2018YJS124, 2018JBZ106 and 2017JBM089, National Natural Science Foundation of China under Grant Nos. 51678030, 51608031 and 51708020, the Science and Technology Foundation of Tsinghai Province (2017-SF-139), the Key Technology R&D Program funded by China Railway Corporation (2017G006-F) and the Transportation Science and Technology Program of Hebei Province (Grant No. QG2018-8).

References

ABAQUS (2014), ABAQUS Standard User's Manual, Version 6.14, Dassault Systemes Simulia Corp., RI, USA.

Amadio, C., Fedrigo, C., Fragiacomo, M. and Macorini, L. (2004), "Experimental evaluation of effective width in steel-concrete composite beams", *J. Constr. Steel. Res.*, **60**(2), 199-220. https://doi.org/10.1016/j.jcsr.2003.08.007

Bathe, K.J. (2014), *Finite Element Procedures*, (Second Edition), Prentice Hall, Upper Saddle River, NJ, USA.

Boules, P.F., Mehanny, S.S.F. and Bakhoum, M.M. (2018), "Shear lag effects on wide U-section pre-stressed concrete light rail bridges", *Struct. Eng. Mech., Int. J.*, **68**(1), 67-80. https://doi.org/ 10.12989/sem.2018.68.1.067

Cao, G.H. and Fang, Z. (2006), "Mechanical Behaviors Test of RC Continuous Box Girder with Wide Flange", *China Journal of Highway and Transport*, **19**(5), 46-52. (in Chinese)

CEB-FIP (2010), Model Code 2010, First complete draft, vol. 1, International Federation for Structural Concrete (fib), Lausanne, Switzerland.

Chen, J., Shen, S.L., Yin, Z.Y. and Horpibulsuk, S. (2014), "Closed-form solution for shear lag with derived flange deformation function", *J. Constr. Steel. Res.*, **102**, 104-110. https://doi.org/10.1016/j.jcsr.2014.07.003.

Dezi, L., Gara, F. and Leoni, G. (2003), "Shear-lag effect in twin-girder composite decks", *Steel Compos. Struct.*, **3**(2), 111-122. https://doi.org/10.12989/scs.2003.3.2.111

Eurocode (2004), Design of Composite Steel and Concrete Structures. Part 1.1: General Rules and Rules for Buildings, European Committee for Standardization; Brussels, Belgium.

Gandelli, E., Penati, M., Quaglini, V., Lomiento, G., Miglio, E. and Benzoni, G.M. (2019), "A novel OpenSees element for single curved surface sliding isolators", *Soil Dyn. Earthq. Eng.*, **119**, 433-453. https://doi.org/10.1016/j.soildyn.2018.01.044

Gara, F., Leoni, G. and Dezi, L. (2009), "A beam finite element including shear lag effect for the time-dependent analysis of steel-concrete composite decks", *Eng. Struct.*, **31**(8), 1888-1902. https://doi.org/10.1016/j.engstruct.2009.03.017

Hognestad, E., Hanson, N.W. and McHenry, D. (1955), "Concrete stress distribution in ultimate strength design", *ACI J. Proceedings*, **52**(12), 455-480.

JTG D60-2015 (2015), General specifications for design of highway bridges and culverts, Ministry of Transport of PRC, Beijing, China. [In Chinese]

Lacki, P., Nawrot, J., Derlatka, A. and Winowiecka, J. (2019), "Numerical and experimental tests of steel-concrete composite beam with the connector made of top-hat profile", *Compos. Struct.*, **211**, 244-253. https://doi.org/10.1016/j.compstruct. 2018.12.035

Lin, P., Fang, W.B., Yang, Z.J., Sun, L.X. and Ji, W. (2015), "Shear lag effect analysis of box girder bridge under prestressing effect", *China J. Highway Transport*, **28**(5), 101-107. [In Chinese]

Luo, Q.Z., Wu, Y.M., Tang, J. and Li, Q.S. (2002a), "Experimental studies on shear lag of box girders", *Eng. Struct.*, **24**(4), 469-477. https://doi.org/10.1016/S0141-0296(01)00113-4

Luo, Q.Z., Tang, J., Li, Q.S. (2002b), "Finite segment method for shear lag analysis of cable-stayed bridges", *J. Struct. Eng.*, **128**(12), 1617-1622. https://doi.org/10.1061/(ASCE)0733-9445(2002)128:12(1617)

Luo, D., Zhang, Z. and Li, B. (2019), "Shear lag effect in steel-concrete composite beam in hogging moment", *Steel Compos. Struct., Int. J.*, **31**(1), 27-41. https://doi.org/10.12989/scs.2019.31.1.027

Ma, Y., Ni, Y.S., Xu, D. and Li, J.K. (2017), "Space grid analysis method in modelling shear lag of cable-stayed bridge with corrugated steel webs", *Steel Compos. Struct., Int. J.*, **24**(5), 549-559. https://doi.org/10.12989/scs.2017.24.5.549

Nie, J.G. and Tao, M.X. (2012), "Slab spatial composite effect in composite frame systems. I: Effective width for ultimate loading capacity", *Eng. Struct.*, **38**, 171-184. https://doi.org/10.1016/j. engstruct.2011.11.034

Nie, J.G., Tao, M.X., Cai, C.S. and Chen, G. (2011), "Modeling and investigation of elasto-plastic behavior of steel–concrete composite frame systems", *J. Constr. Steel. Res.*, **67**(12), 1973-1984. https://doi.org/10.1016/j.jcsr.2011.06.016

Reissner, E. (1946), "Analysis of shear lag in box beams by the principle of minimum potential energy", *Q. Appl. Math.*, **4**(3), 268-278. https://doi.org/10.1090/qam/17176

Tao, M.X. and Nie, J.G. (2014), "Fiber beam-column model considering slab spatial composite effect for nonlinear analysis of composite frame systems", *J. Struct. Eng.*, **140**(1), 04013039. https://doi.org/10.1061/(ASCE)ST.1943-541X.0000815

Vojnić-Purčar, M., Prokić, A. and Bešević, M. (2019), "A numerical model for laminated composite thin-walled members with openings considering shear lag effect", *Eng. Struct.*, **185**, 392-399. https://doi.org/10.1016/j.engstruct.2019.01.142

Wendner, R., Vorel, J., Smith, J., Hoover, C.G., Bažant, Z.P. and Cusatis, G. (2015), "Characterization of concrete failure behavior: a comprehensive experimental database for the calibration and validation of concrete models", *Mater. Struct.*, **48**(11), 3603-3626. https://doi.org/10.1617/s11527-014-0426-0

Zhang, Y.H. and Lin, L.X. (2014), "Shear lag analysis of thin-walled box girders adopting additional deflection as generalized displacement", *J. Eng. Mech.*, **104**(4), 04014005. https://doi.org/10.1061/(ASCE)EM.1943-7889.0000705

Zhou, S.J. (2010), "Finite beam element considering shear-lag effect in box girder", *J. Eng. Mech.*, **136**(9), 1115-1122. https://doi.org/10.1061/(ASCE)EM.1943-7889.0000156

Zhou, G., Li, A., Li, J., Duan, M., Spencer, B.F. and Zhu, L. (2018), "Beam finite element including shear lag effect of extra-wide concrete box girders", *J. Bridge Eng.*, **23**(11), 04018083. https://doi.org/10.1061/(ASCE)BE.1943-5592.0001297

Zhu, L. and Su, R.K.L. (2017), "Analytical solutions for composite beams with slip, shear-lag and time-dependent effects", *Eng. Struct.*, **152**, 559-578. https://doi.org/10.1016/j. engstruct.2017.08.071

Zhu, L., Nie, J.G., Li, F.X. and Ji, W.Y. (2015), "Simplified analysis method accounting for shear-lag effect of steel–concrete composite decks", *J. Constr. Steel. Res.*, **115**, 62-80. https://doi.org/10.1016/j.jcsr.2015.08.020

CC